J Mater Sci (2010) 45:5993–6008
DOI 10.1007/s10853-010-4849-x

REVIEW

Review on oxides of antimony nanoparticles: synthesis, properties, and applications

Hui Shun Chin · Kuan Yew Cheong · Khairunisak Abdul Razak

Received: 31 May 2010 / Accepted: 18 August 2010 / Published online: 3 September 2010

Abstract In this article, synthesis methods, properties, and applications of antimony oxide nanoparticles are reviewed. Oxides of antimony exist in three phases, namely antimony trioxide, antimony tetroxide, and antimony pentoxide. Physical and optical properties of these nanoparticles are reviewed and compared with their bulk forms. According to literature works, a total of eight synthesis methods have been used to produce these nanoparticles. The size, distribution, shape, and structure of the nanoparticles which are synthesized by different methods are compiled and compared. It is reported that the properties are strongly dependent on the synthesis methods. Advantages and disadvantages of each synthesis method are discussed and compared. Most literatures report on the optical and physical properties of the nanoparticles. Reports on the electrical properties are scarce. As the applications of these nanoparticles cover a wide range, several challenges must be overcome to use them well. These challenges are also being presented and explained in this article.

Introduction

Oxide nanoparticles have received considerable attention over the last few decades for scientific research and technological applications. This is largely related to the exhibition of novel properties by the nanostructure materials when compared with the bulk materials [1, 2]. It is well known that the fundamental properties of the nanostructure materials depend strongly on their sizes and shapes [3, 4]. Therefore, researchers have placed much effort into controlling the desired morphologies of these nanostructure materials [5–14].

Oxides of antimony (OA) are a key member among all the other metal oxides from V to VI groups [15]. Literature [16] reports that there are three phases of well-indentified OA, which are antimony trioxide (Sb_2O_3), antimony tetroxide (Sb_2O_4), and antimony pentoxide (Sb_2O_5). The change in Gibbs energy is the key parameter that affects the formation of the desired phase [17–20]. For instance, Sb_2O_5 does not exist above 525 °C, only Sb_2O_3 and Sb_2O_4 are formed. Literature proves that nanoparticles of OA possess excellent properties as compared to bulk OA, for example, a higher refractive index [21, 22], higher abrasive resistance, higher proton conductivity [23, 24], excellent mechanical strength [25], and higher absorbability [26].

In general, OA nanoparticles can be synthesized via several methods, which can be classified according to the starting material for synthesizing nanoparticles. There are three main groups of starting material namely antimony trichloride ($SbCl_3$), antimony (Sb), and slag. For $SbCl_3$ as a starting material, microemulsion [27], solution phase reduction [28], hydrothermal [29–32], γ-ray radiation–oxidization [33, 34], and biosynthesis [35, 36] methods have been used. On the other hand, pure Sb is used as a precursor to synthesize OA nanoparticles via a hybrid induction method and laser heating (HILH) [26, 37–42] as well as thermal oxidation [43]. Furthermore, vacuum evaporation [44] method using slag as starting material has been reported as potential solutions for producing OA nanoparticles. However, there are some limitations associated with these methods mainly due to the high

H. S. Chin · K. Y. Cheong (✉) · K. A. Razak
Energy Efficient & Sustainable Semiconductor Research Group, School of Materials and Mineral Resources Engineering, Universiti Sains Malaysia, 14300 Nibong Tebal, Penang, Malaysia
e-mail: cheong@eng.usm.my

temperature and high pressure for hydrothermal synthesis [32] and complicated techniques for the γ-ray radiation–oxidization route [33].

In view of the unique properties of OA nanoparticles, a few technological applications have been raised eventually. These applications can be grouped into three fields, namely, chemical, sensing, and semiconductors. In the chemical field, OA nanoparticles are useful as a flame retardant synergist using it together with halogenated compounds in plastics, paints, adhesives, sealants, rubbers, and textile back coatings [45–51]. In addition, OA nanoparticles also possess a remarkable catalytic property in poly(ethylene terephthalate) (PET) and organic synthesis industries [52–56]. Further established uses of OA nanoparticles include as a clarifying agent [57, 58], opacifier [59], filling agent [60], pigments, and medicine [35] in the chemical field. In the sensing field, OA nanoparticles are found to possess high proton conductivity properties, making it potentially useful as a promising humidity sensing material [23, 24]. In the semiconducting field, extremely fine particles of colloidal OA are used as optical materials due to their high refractive index and high abrasive resistance [21, 22].

This article aims to review various types of methods to synthesis OA nanoparticles, its outcomes and challenges faced during synthesizing. At the same time, properties of the different phases of OA (bulk), as well as a comparison of properties between nanoparticles and bulk OA are being addressed. Taking into consideration the excellent properties being demonstrated, some of the potential applications of OA nanoparticles are being reported.

Phases and properties

Phases

Massalski et al. [16] identified three main phases of OA, namely, Sb_2O_3, Sb_2O_4, and Sb_2O_5. Typically, Sb_2O_3 has two crystalline modifications, cubic polymorph (senarmontite stable phase) and orthorhombic polymorph (valentinite metastable phase) [61]. It was found that orthorhombic polymorph can be transformed into cubic polymorph at 490–530 °C [62]. In addition, senarmontite exists as a low temperature α-phase and valentinite as a high temperature β-phase [63, 64]. The differences of both polymorphs lie in their different physicochemical properties.

Formation of the three phases is controlled by the reaction of both thermodynamic and kinetic activities of the metal and oxides, which is related directly to the change in Gibbs energy [17–20]. For example, Sb_2O_5 does not form above 525 °C, and thus, only both Sb_2O_3 and SbO_2 (Sb_2O_4) exist. According to the theory of oxidation, a multilayer scale will form on the metal when more than one type of oxide coexists with the metal in the system [19]. The multilayer scale described by varying oxygen content, from metal-rich oxides (low oxygen equilibrium pressure) to oxygen-rich oxides (high oxygen equilibrium pressure) is shown in Fig. 1a. At the same time, SbO_2 will be further oxidized in air to form a much more stable oxide, which is Sb_2O_3 (Fig. 1b).

On the other hand, Sb_2O_5 can be prepared by oxidizing antimony with concentrated nitric acid and the prepared Sb_2O_5 is normally in hydrated state [61]. Sb_2O_4 is a compound of Sb_2O_3 and Sb_2O_5, where it contains mixed valence of Sb(III) and Sb(V). The two stable modifications of Sb_2O_4 are the room temperature orthorhombic α-phase (cervantite) and high temperature monoclinic β-phase [65]. Hence, Sb_2O_4 can be obtained by two possible routes, either heating Sb_2O_3 in air or prolonged heating hydrated Sb_2O_5 at 800 °C, as shown in Eqs. 1 and 2 [61].

$$Sb_2O_3 + 0.5O_2 \rightarrow Sb_2O_4 \quad \Delta H = -187\,\text{kJ/mol} \tag{1}$$

$$Sb_2O_5 \rightarrow Sb_2O_4 + 0.5O_2 \quad \Delta H = -64\,\text{kJ/mol} \tag{2}$$

Properties

Table 1 [61] presents various properties of the three phases of OA (Sb_2O_3, Sb_2O_4, and Sb_2O_5) in the bulk form. In general, OA appears as a solid or powder ranging from white to yellow in color. These are the white solid (Sb_2O_3), white or yellow solid (Sb_2O_4), and yellow solid (Sb_2O_5). The densities of OA phases will sequence from Sb_2O_3, Sb_2O_4, and Sb_2O_5 are 5.2, 6.64, and 3.78 g/cm^3, respectively. Sb_2O_3 melts at 636 °C and boils at 1425 °C, in which the melting point is higher than that of Sb_2O_5 which is 380 °C. Based on the solubility in water only Sb_2O_5 is reported to be very soluble when compared to both Sb_2O_3

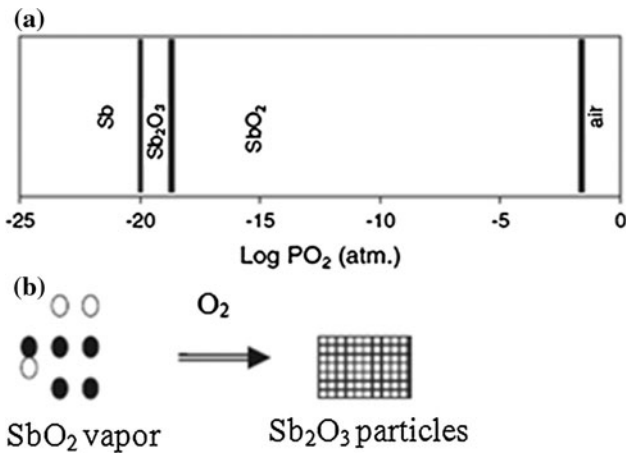

Fig. 1 Illustration of the formation of **a** multilayer scale on metal Sb, **b** stable Sb_2O_3 particles [43]

Table 1 Summary properties of three phases of OA in bulk [61]

Properties	Sb_2O_3	Sb_2O_4	Sb_2O_5
Appearance	White solid	White or yellow solid	Yellow solid
Molecular weight (g/mol)	291.52	307.52	323.52
Density (g/cm^3)	5.2	6.64	3.78
Melting point (°C)	656	N/A	380
Boiling point (°C)	1425	N/A	N/A
Crystal structure	Cubic (<570 °C)	Orthorhombic	N/A
	Orthorhombic (>570 °C)	Monoclinic	
Solubility in water	Insoluble	Insoluble	Very slightly soluble

and Sb_2O_4, which are insoluble in water. Sb_2O_3 exists in two forms, cubic and orthorhombic. When heating is carried out above 570 °C, orthorhombic Sb_2O_3 is formed and cubic Sb_2O_3 will be formed when heating is conducted below 570 °C.

Researchers reported that OA nanoparticles possess novel or excellent properties when compared to bulk OA [1–3], some of the studied properties are summarized in Table 2. By definition, nanoparticles have sizes <100 nm with a much bigger surface area as compared to bulk materials. In flame-retardant manufacturing, impact strength and translucent are two main properties that affect the quality of the products [49]. The bulk OA contributes to higher losses in translucency, which restricts the range of available color choices. It is because higher colorant loading is required to counterbalance the tinting effect of OA. Using nanoparticles of OA, colorant loadings can be abridged one-third to one-half of the normal quantity utilized. Thus, it helps in reducing the manufacturing cost and improves the properties or quality of the products. Consequently, the mechanical properties (impact strength and tensile strength) of OA nanoparticles are improved [25]. In conjunction with the bigger surface area of OA nanoparticles, it has strong absorption property [26] for metallic impurities, thus enhancing the performance of the epoxy in electronic applications. Furthermore, Lie et al. [66] reported that OA nanoparticles behave stable superhydrophobic properties with a small sliding angle (5°) when compared to bulk OA, where this will expand the existing applications of OA.

By investigating the photoluminescence properties of OA nanoparticles, it indicated strong emission band at 374 nm with an optical bandgap $E_g = 3.3$ eV, which are located in the near-ultraviolet (UV) region [60]. Besides, the quantum effect of the OA nanoparticles will enhance the UV absorbance of OA [67]. Therefore, it could be used in a UV light emitting device (LED) and in solar cell technology [68]. Moreover, Chen et al. [32] claimed that OA nanoparticles exhibited a significant red shift (2.32–3.33 eV) in emission band, as compared to bulk OA (4.31 eV), which suggested potential usage in optoelectronic devices. On the other hand, OA nanoparticles-based glasses exhibited extended infrared transmission, higher refractive index, and higher abrasive resistance, as compared to borosilicates [21, 22]. For instance, orthorhombic phase of OA nanoparticles is a main component in Sb_2O_3–B_2O_3 glasses, where it helps in improving the non-linear optical properties [69].

In term of sensing perspective, OA nanoparticles possess both humidity and gas-sensing properties. Owing to its higher proton conductivity properties when compared to bulk form, OA nanoparticles are found to be a potential humidity sensor. Ozawa et al. [23] and Dzimitrowicz et al. [24] investigated that the electrical conductivity of OA

Table 2 Comparison properties of both bulk and nanoparticles of OA [21–26, 49, 66–68, 95]

Properties	OA-bulk	OA-nanoparticles
Particle size	>100 nm	<100 nm
Translucent	Maximum loss	Minimum loss
Colorant loading	Higher	Reduced half of bulk
Impact strength	Lower	Higher
Tensile strength	Lower (<4.05 MPa)	Higher (4.05–9.35 MPa)
Absorbability	Weak	Strong
Superhydrophobic	Unstable (sliding angle > 5°)	Stable (sliding angle < 5°)
Refractive index	Lower (<2)	Higher (>2)
Abrasive resistance	Lower	Higher
UV vis absorbance	Lower (<0.3 a.u of absorbance)	Higher (>0.3 a.u of absorbance)
Proton conductivity	Lower (<2.89 × 10^{-3} S/cm)	Higher (2.89 × 10^{-3} S/cm)

Table 3 Summary of varies synthesis methods of Sb_2O_3 nanoparticles

Starting material	Synthesis methods	Size (nm)	Size distribution	Shape	Structure	Limitations	References
$SbCl_3$	Microemulsion	10–80	Random	Polyhedral	Cubic (FCC)	Required heating to 350 °C to get powder	[27]
	Solution phase reduction	17 ± 1	Uniform	Spherical	Cubic (FCC)	Required stirring for 24 h	[28]
	Hydrothermal	~500	N/A	Spherical	Cubic (FCC)	Required heating for 12 h	[32]
		<100	Uniform	N/A	Orthorhombic		
	γ-Ray radiation–oxidization	8–48	N/A	Spherical	Cubic (FCC)	Complex techniques	[33]
	Biosynthesis	2–10	Uniform	Spherical	Cubic (FCC)	Longer processing time (~6 days)	[35, 36]
Sb	Hybrid induction and laser heating (HILH)	80	Uniform	Spherical	Cubic (FCC)	Obtained mixture of Sb and Sb_2O_3 nanoparticles Expensive experimental setup	[37, 38]
	Thermal oxidation	10–100	Random	Polyhedral	Cubic (FCC)	Required minimum deposition time for 4 h	[43]
Slag	Vacuum evaporation	<100	Uniform	Spherical	Cubic (FCC)	High temperature (893 K) and high pressure (250 Pa)	[44]

increases from 1.69×10^{-5} to 2.89×10^{-3} S/cm as the relative humidity altered from 11 to 85%. In the case of gas-sensing properties, OA-based gas sensor prepared by metal organic chemical vapor deposition (MOCVD) method, indicated a great response to methane gas and fully recovered once the removal of the gas [70]. By preparing via screen printing method, OA-based gas sensor exhibited fast response to 100 ppm of ethanol at operating temperature of 500 °C. Meanwhile, OA-based gas sensor also behaved quick recovery, when changing from ethanol flow to clean air flow [70].

Synthesis methods

There are few methods that have been reported to synthesis OA nanoparticles, which can be categorized into three groups according to the starting material during synthesis. The three groups are: $SbCl_3$, Sb, and slag as starting materials. The details of the synthesis methods are reviewed in the subsequent paragraphs and are summarized in Table 3.

Starting material: $SbCl_3$

Microemulsion

Zhang et al. [27] reported the synthesis of OA nanoparticles via microemulsion method using polyvinyl alcohol (PVA). There are two main functions of PVA in this method: one is to prevent agglomeration of the formed nanoparticles, and the other is to form a spherical reactor. In this method, a 228 mg of $SbCl_3$ as a starting material was dissolved into 100 mL of hydrochloride acid solution (1 M). After dissolving, 3 g of PVA was added. Then the mixture was ultrasonically vibrated for 15 min, followed by dropping 12 mL of sodium hydroxide (NaOH) into the mixture slowly until the mixture turns to transparent pale yellow color. In order to bring about a more intense color, the solution was refluxed for 1 h. During refluxing, the solvent was evaporated at 80 °C at in a reduced atmosphere. The final product, which was in the form of dry powders were obtained by heating the solvent at 350 °C under an ambient atmosphere for 1 h.

Transmission electron microscope (TEM) analysis revealed that the nanoparticles are in polyhedral shape while their sizes range from 10 to 80 nm (Fig. 2). The difference in shape and size of the nanoparticles is mainly

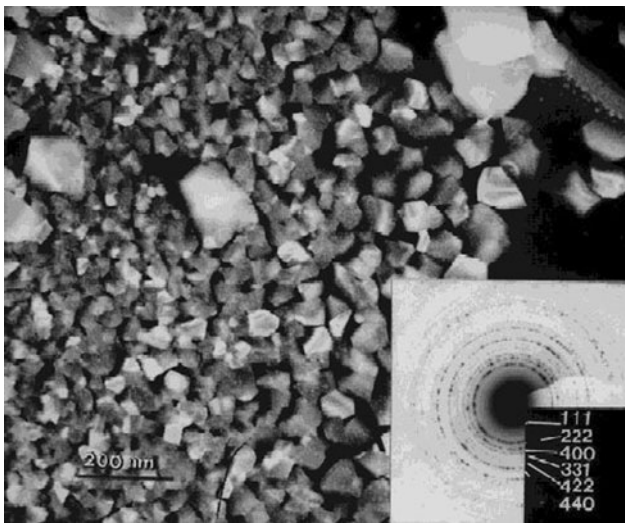

Fig. 2 TEM micrograph showing the morphology of antimony oxide nanoparticles and the corresponding SAED is inserted at the *right bottom corner* [27]

Table 4 Comparison between the experimental planar spacing and the standard data from JCPDS card [27]

Radium (mm)	d_{exp}	d_{cal}	(*hkl*)	Relative intensity
$R_1 = 1.98$	6.35	6.439	(111)	15
$R_2 = 3.90$	3.17	3.219	(222)	100
$R_3 = 4.50$	2.75	2.788	(400)	33
$R_4 = 4.87$	2.54	2.558	(331)	8
$R_5 = 5.60$	2.21	2.2765	(422)	1
$R_6 = 6.40$	1.93	1.9714	(440)	33
$R_7 = 7.50$	1.65	1.6812	(622)	30

d_{cal} from the JCPDS card

due to the growth process of the nanoparticles, in which they begin to grow in a different stages and periods. Furthermore, the selected area electron diffraction pattern (SAED) inserted at right bottom corner of Fig. 2 shows that the nanoparticles consist of many reflection rings, which means the structure of nanoparticles are polycrystalline. Table 4 shows the comparison of experimental planar spacing and the standard data from JCPDS card (43-1071). It is observed that both planar spacing are well consistent with cubic Sb_2O_3, which has the space group *Fd*3*m*. Large-angle tilting diffraction patterns on a larger antimony oxide nanoparticle (~60 nm) as shown in Fig. 3 show that the crystal structure of nanoparticles is face-centered cubic (FCC).

In summary, this method is a simple way to synthesis of OA nanoparticles using PVA through a reaction between $SbCl_3$ and NaOH [27]. The achieved sizes of the nanoparticles are range from 10 to 80 nm in polyhedral forms. SAED revealed that the nanoparticles are polycrystalline in structure. From characterization, it can be concluded that the nanoparticles are mainly Sb_2O_3 cubic (FCC) structure.

Solution phase reduction

Ye et al. [28], on the other hand, reported the successful synthesis of Sb_2O_3 nanoparticles using *cetyltrimethylammonium bromide* (CTAB) as a soft template and employing $Sb(OH)_4^-$ as an inorganic precursor (formed by controlling pH of the $SbCl_3$ solution to value of 14 [71]). In this solution phase reduction method, 0.15 mmol (or even less) of CTAB was added into a 100-mL solution of 0.01-M $SbCl_3$ under constant stirring for 2 h until CTAB is dissolved fully. In order to reach a pH value of 14, 1 M of NaOH solution was added dropwise to the above mixture. Subsequently, the resulting solution was stirred for 24 h at room temperature, followed by putting it into an oven at 60 °C for 4 h. After heating was completed, the light brown precipitate was centrifuged and washed multiple times using ethanol and distilled water. Then, the precipitate was dried under vacuum at room temperature gradually.

In Fig. 4, Sb_2O_3 nanoparticles in spherical shape with a narrow size distribution or having a diameter of 17 ± 1 nm were observed under the scanning electron microscope (SEM). These morphologies can be explained in terms of the CTAB concentration, where lower CTAB concentration favors the lowest order phase such as the spherical

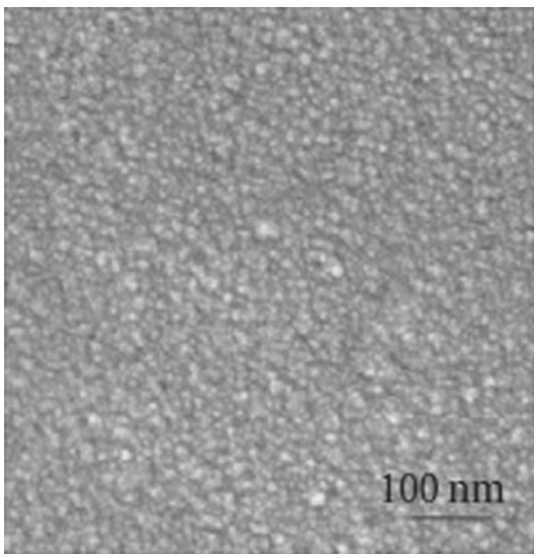

Fig. 4 SEM image of Sb_2O_3 nanoparticles obtained by CTAB [28]

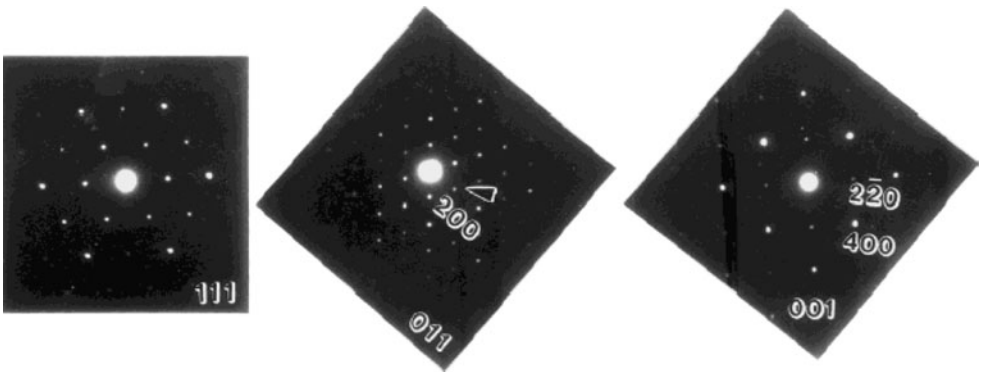

Fig. 3 Large-angle tilting diffraction patterns on a larger antimony oxide particle (~60 nm) [27]

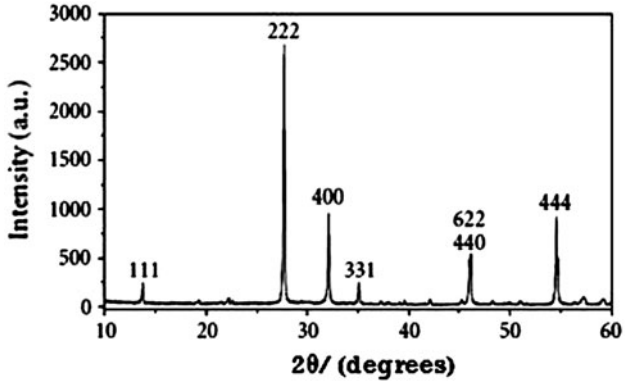

Fig. 5 XRD spectrum of Sb_2O_3 cubic phase [28]

shape structure and higher CTAB concentration contributes to a higher ordered phase such as nanowires and nanoribbons [72–75]. The electrostatic interaction between $Sb(OH)_4^-$ anions and CTAB cations formed CTA^+–$Sb(OH)_4^-$ ion pairs [76]. The lower concentrations of CTA^+ cations caused the necessary charge compensating anions to decrease, and led the system to find its minimum energy configuration by adopting the spherical structure [77]. Therefore, Sb_2O_3 nanoparticles were formed after the subsequent thermal treatment. In order to understand the crystal structure and phase of the nanoparticles, X-ray diffraction (XRD) was carried out. From the diffraction peak in the XRD spectrum as shown in Fig. 5, it was concluded that the Sb_2O_3 nanoparticles were in cubic phase according to the literature (JCPDS card 42-1466). Meanwhile, the XRD results also indicated that no other phases were detected from the spectrum.

In conclusion, Sb_2O_3 cubic phase nanoparticles with narrow distribution (17 ± 1 nm) and spherical shape were successfully synthesized by adopting CTAB as soft template. The advantages of this method are easy handling, relatively low cost, and large-scale production. The control of the CTAB concentration to synthesize Sb_2O_3 nanostructures is beneficial in flame-retardant and catalyst applications. Furthermore, this facile synthesis method could be explored to synthesize other nanostructures, such as SnO_2 [78].

Hydrothermal

Chen et al. [32] studied the preparation of antimony oxide nanoparticles via a hydrothermal method. Both cubic and orthorhombic phase of Sb_2O_3 nanoparticles can be obtained by varying the solvent composition, such as ethylene glycol (EG)–water (H_2O) and toluene–H_2O. Besides, the control of pH value is an important parameter to determine the morphologies of the nanostructures. In this method, 2 mmol of $SbCl_3$ was dissolved in 20 mL of EG solution under vigorous stirring to form a transparent solution. Subsequently, 20 mL of distilled water was added to the above solution to obtain a lacteous colloid. Then, the resulting mixture was stirred for 15 min and 6 M of NaOH solution was added to adjust the pH value in the range of 8–9. The whole solution was stirred for another 20 min before being transferred into a 100-mL Teflon-lined stainless steel autoclave. The autoclave was sealed and kept at 120 °C. After 12 h, the resulting white product was centrifuged and washed several times with distilled water and ethanol, and then vacuum dried at 60 °C for 6 h. In order to investigate the effect of solvent composition on the phase formation of Sb_2O_3 nanoparticles, the same procedures were repeated by replacing EG solution with toluene solution.

XRD was used to observe the phase presence, crystallinity, and purity of the samples which were synthesized in both EG–H_2O and toluene–H_2O at 120 °C for 12 h. The reflection spectrums in both Figs. 6 and 7 could be directly indexed as cubic Sb_2O_3 (JCPDS card 5-534) and orthorhombic Sb_2O_3 (JCPDS card 11-689), respectively. Furthermore, no other phases existed in both spectrums, which strongly suggested the formation of pure cubic Sb_2O_3 and orthorhombic Sb_2O_3 in pH 8–9. From the XRD spectrums, solvent composition is critical to control the phase of Sb_2O_3. TEM image in Fig. 8 displays the morphology of sub-micronmeter ($\sim$500 nm) cubic (FCC) Sb_2O_3 particles which are almost spherical shape. Figure 9 shows the corresponding HRTEM image obtained at the edge of the Sb_2O_3 nanoparticle, broad lattice spaces of 0.32 and 0.64 nm are found and matched the (222) and (111) planes, which are indicated in the inserted SAED image. Tiny orthorhombic Sb_2O_3 nanoparticles (<100 nm) are revealed in Fig. 10 which were obtained at pH 8–9 in toluene–H_2O. From the nanostructure synthesis perspective, EG is well known to support two functions: one as a reducing agent to prepare metal or alloy nanoparticles, and the other one as

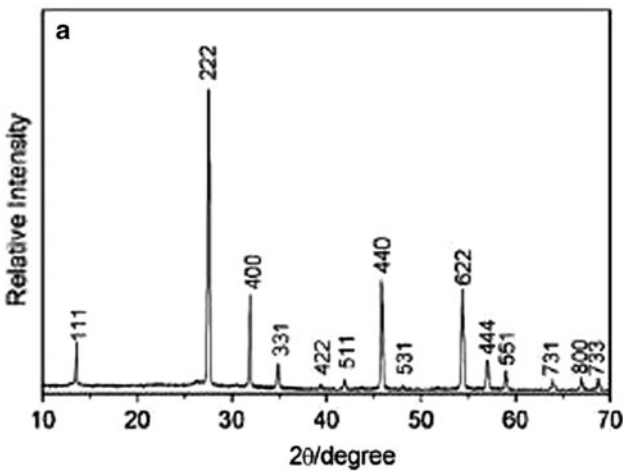

Fig. 6 XRD spectrum of the sample obtained in EG–H_2O [32]

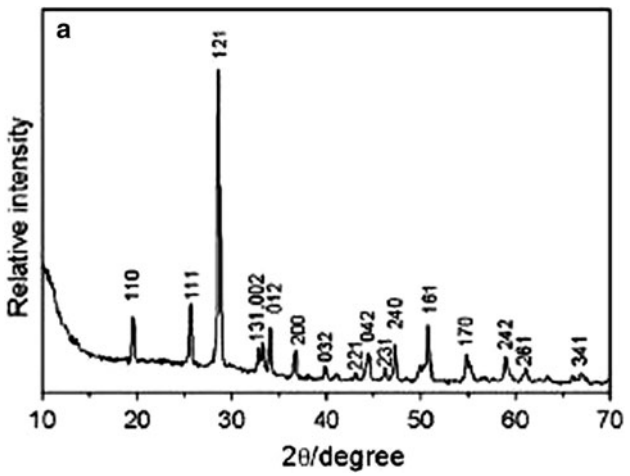

Fig. 7 XRD spectrum of the sample obtained in toluene–H_2O [32]

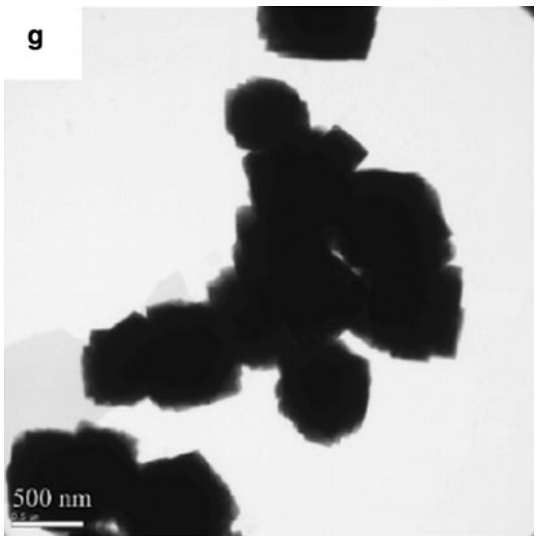

Fig. 8 TEM image of sample obtained in EG–H_2O [32]

coordination agent or temporary ligand in the synthesis of SnO_2, TiO_2, PbO, and In_2O_3 nanoparticles [79–81]. The chelating ligand EG binds strongly to metal to form a more stable complex, whereas the nonchelating ligand toluene binds weakly to the metal. The different capability in its ability to bind with metal contributed to the formation of different phases of Sb_2O_3 nanoparticles. Thus, cubic Sb_2O_3 and orthorhombic Sb_2O_3 can be synthesized by choosing a proper solvent composition.

In summary (Table 5), the sizes and phases of nanoparticles in this study were strongly affected by the solvent composition and pH of the reaction mixture [32]. In this content, Sb_2O_3 nanoparticles were synthesized at pH 8–9 in both EG–H_2O and toluene–H_2O. EG–H_2O favored the formation of cubic Sb_2O_3 nanoparticles whereas toluene–H_2O favored the formation of orthorhombic Sb_2O_3 nanoparticles.

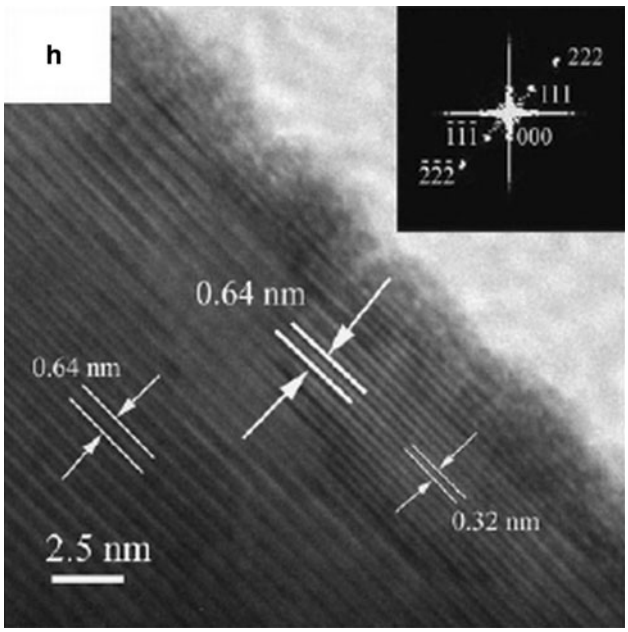

Fig. 9 HRTEM SAED image of sample obtained in EG–H_2O [32]

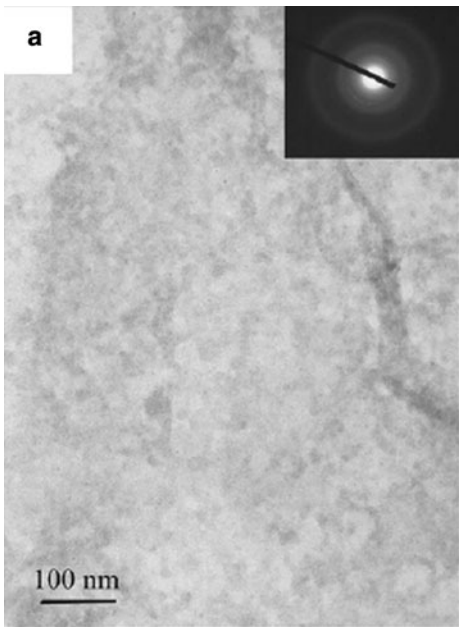

Fig. 10 TEM image of sample obtained in toluene–H_2O [32]

Table 5 Summary of Sb_2O_3 particles obtained at 120 °C for 12 h in mixed solvents [32]

Product	pH	Solvent composition	Phase	Size (nm)
Sb_2O_3	8–9	EG–H_2O	Cubic (FCC)	~500
		Toluene–H_2O	Orthorhombic	<100

γ-Ray radiation–oxidization

Liu et al. [33] discovered γ-ray radiation–oxidization to synthesize Sb_2O_3 nanoparticles from aqueous solutions at room temperature and ambient pressure. Particle size and yield rate were mainly affected by the concentration of $SbCl_3$, radiation dose, kind, and concentration of the surfactant. The experiment started by adding $SbCl_3$ in distilled water, followed by dropping NaOH to dissolve the white precipitate which came from Sb^{3+} hydrolysis in water. Two types of surfactants were selected in this study, which were PVA and sodium dodecyl sulfate (SDS), and isopropanol acting as a scavenger for hydroxyl radicals. The dissolved oxygen was removed by bubbling it with nitrogen gas for 30 min. Subsequently, the mixture solution was irradiated with γ-ray in a field of a 70000Ci ^{60}Co γ-ray source. After separating the precipitate, it was washed with distilled water and alcohol, and then dried under oxygen or air atmosphere at 60 °C in a drier. The Sb_2O_3 nanoparticles were black in color.

Table 6 summarizes the experimental conditions and the experimental results of preparing Sb_2O_3 nanoparticles. The XRD spectrum in Fig. 11 shows that nanoparticles are pure Sb_2O_3 nanoparticles, and no other phases are observed. The average particle size of nanoparticles can be calculated by adopting the Scherrer formula: $L = (K\lambda)/(\beta\cos\theta)$, where L is the average particle size, K is the Scherrer constant related with the shape and (hkl) of crystals [82], λ is the wavelength ($\lambda = 1.5418$ Å) of X-ray, and β is obtained from the Warren and Biscoe equation [83]: $\beta_2 = B_2 - b_2$, where B and b are the angular half widths for the experimental samples and for the standard sample, respectively. From the XRD spectrum, the calculated particle size is 19 nm. TEM images in Fig. 12 displays both sample 2 and 8 particles having quasi-spherical shapes.

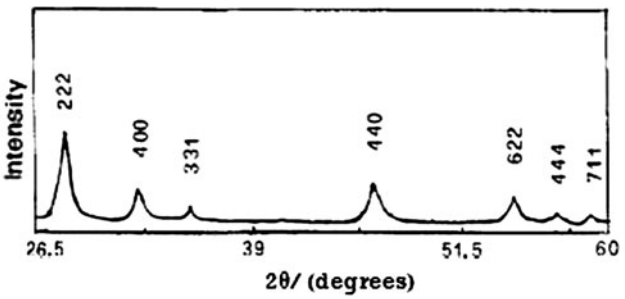

Fig. 11 XRD spectrum of Sb_2O_3 nanoparticles (sample 2 in Table 6) [33]

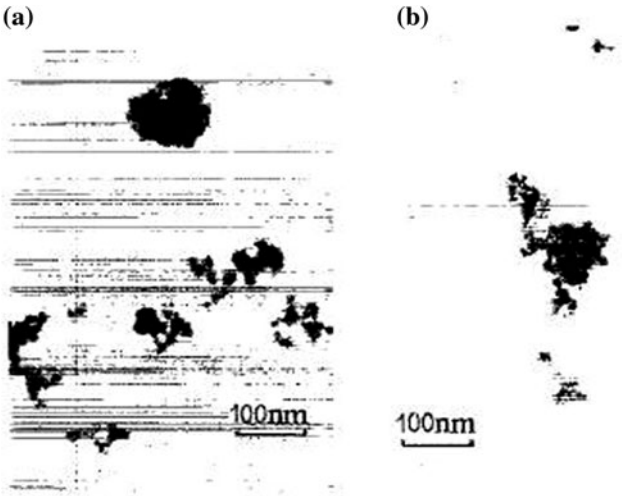

Fig. 12 TEM images of Sb_2O_3 nanoparticles; **a** samples 2 and **b** 8 (from Table 6) [33]

Table 6 The correlation between the experimental conditions and the experimental results [33]

Sample	Concentration of $SbCl_3$ (M)	Surfactant	Radiation dose ($\times 10^4$ Gy)	Average particle size (nm)	Yield rate (%)
1	0.005	0.1% PVA	5.3	15	–
2	0.01	0.1% PVA	5.3	19	54
3	0.015	0.1% PVA	5.3	21	–
4	0.02	0.1% PVA	5.3	21	–
5	0.03	0.1% PVA	5.3	22	50
6	0.01	0.01% PVA	5.3	42	–
7	0.01	0.05% PVA	5.3	33	–
8	0.01	0.2% PVA	5.3	8	–
9	0.01	0.01% SDS	5.3	25	–
10	0.01	0.04% SDS	5.3	8	–
11	0.01	0.1% PVA	6.24	34	64
12	0.01	0.1% PVA	8.03	48	72

From Table 6, there are three parameters affecting the particle size and yield rate of Sb_2O_3 nanoparticles, which are concentration of $SbCl_3$, radiation dose, types and composition of surfactants. Results revealed that the increase in concentration of $SbCl_3$ and radiation dose contributed to an increase in the average particle size of Sb_2O_3 nanoparticles. In addition, the increase of radiation dose caused the yield rate to increase. Surfactant (PVA and SDS) was applied to prevent aggregation and growth of particles in solutions, where the surfactant molecules coat the particles and subsequently separate each of the particles. Results indicated that smaller particles were produced when higher concentration of surfactant was applied. In this study, PVA is favored as compared to SDS, where SDS could be washed out easily from products.

In conclusion, the γ-ray radiation–oxidization method is beneficial to produce quasi-spherical-shaped particles in the range 8–48 nm [33]. The highest yield rate of 72% can be gained by adopting these conditions: 0.005–0.3 M of $SbCl_3$, 0.01–0.3% of PVA concentration and a radiation dose of 5–8 $\times$ 10^4 Gy. Thus, different sizes of particles can be achieved by controlling three conditions stated above accordingly.

Biosynthesis method

Jha and Prasad [35, 36] reported the successful synthesis of Sb_2O_3 nanoparticles via a biosynthesis method, where yeast was used as starting material. In view of the restrictions of hazardous substances (RoHS) issued by European Union, it is a must to develop a green approach to synthesize nanoparticles. Green approach here means no toxic chemicals are allowed during synthesis of nanoparticles. Literature [35, 36] reviewed that interaction between inorganic nanoparticles and biological structures are one of the most promising areas of research in modern nanoscience and technology. In their study, yeast (*Saccharomyces cerevisiae*) has been selected to study its potential as a putative candidate of fungal genus for the synthesis of Sb_2O_3 nanoparticles. The experiment started by preparing the source culture. The source culture was prepared by allowing the yeast to grow as a suspension culture in the presence of carbon and nitrogen source for 36 h. 25 mL of the culture solution was filtered and diluted four times by adding 30% ethanol solvent (Et-OH). The diluted culture was allowed to grow for another 24 h until a light straw color is observed. After growing for 24 h, 20 mL of $SbCl_3$ (0.025 M) solution was added to the culture solution and the mixture was heated to 60 °C for 10–20 min until a white precipitate was noticed. This indicated the initiation of Sb_2O_3 nanoparticles synthesis. After incubating for 3–4 days at room temperature, coalescent white clusters precipitated at the bottom of the tube.

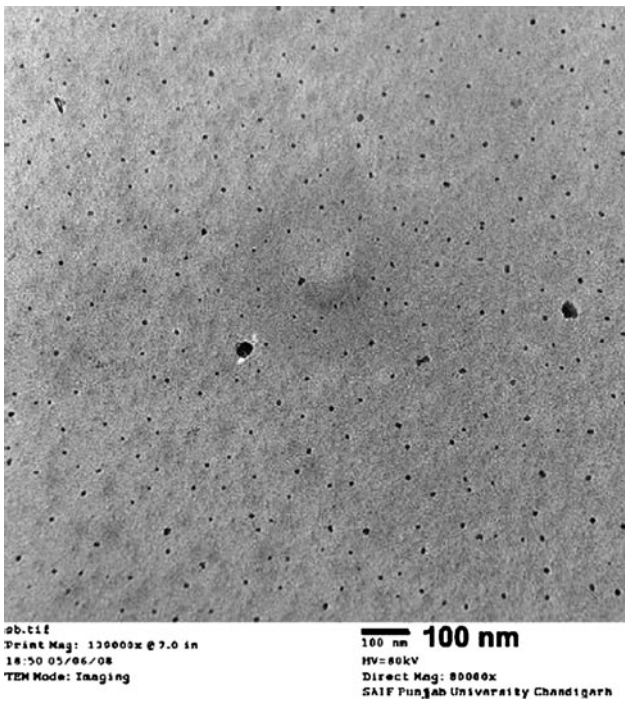

Fig. 13 TEM image of Sb_2O_3 nanoparticles obtained by biosynthesis method [35, 36]

Figure 13 shows the Sb_2O_3 nanoparticles are distributed uniformly with only a few of them showing aggregates of varying sizes as observed under TEM. The TEM image also shows that the Sb_2O_3 nanoparticles are almost in spherical shape and having a size range between 2 and 10 nm. The difference in size is mainly due to the nanoparticles being formed by varying times, where nanoparticles are constrained during nucleating inside the organisms. The mechanism of synthesis Sb_2O_3 nanoparticles is carried out at two distinct levels: (1) tautomerization of quinones are triggered at the cell membrane level once $SbCl_3$ solution is added and (2) oxidases get activated at low value of pH and initiate molecular oxygen for synthesis of Sb_2O_3 nanoparticles. The XRD spectrum of Sb_2O_3

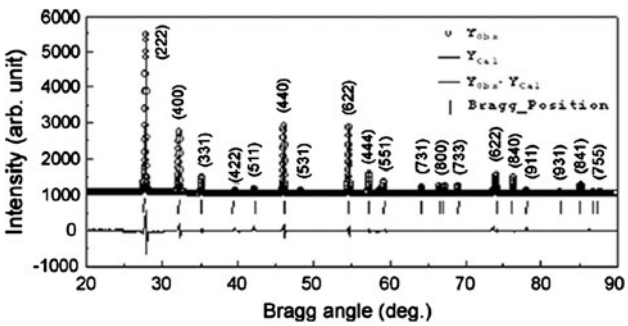

Fig. 14 XRD spectrum of Sb_2O_3 nanoparticles obtained by biosynthesis method [35, 36]

nanoparticles is depicted in Fig. 14. It was found that both the observed and the calculated profile perfectly matched. The XRD spectrum indicated that the sample was in FCC structure of Sb_2O_3 nanoparticles with the lattice parameter: $a = 11.138$ Å, which matched with the literature report (PCPDF Nos: 72-1334 and 75-1565).

The present biosynthesis method is a low-cost green approach, and successfully synthesizes Sb_2O_3 nanoparticles almost spherical in shape and having sizes of 2–10 nm [35]. In this study, yeast is used as starting material to synthesize Sb_2O_3 nanoparticles at room temperature. There are two different mechanisms involved during synthesis of Sb_2O_3 nanoparticles, which are tautomerization of membrane-bound quinines and the pH-sensitive oxidoreductases.

Starting material: Sb

Hybrid induction and laser heating (HILH)

Zeng et al. [37, 38] reported the successful synthesis of Sb_2O_3 nanoparticles with an average size of 80 nm via the HILH method. In this study, Sb_2O_3 nanoparticles were synthesized from pure Sb in the flowing mixture gas of argon (Ar) and oxygen (O_2) environment by the vapor condensation concept. Figure 15 shows the basic experimental setup of this method, where an inductive resource and a continuous wave of carbon dioxide (CO_2) laser beam were hybridized as a heating resource. The whole graphite crucible containing bulk pure Sb (99.5%) was put in a vacuum chamber. Then, the chamber was flowed with a mixture of Ar and O_2 gas at a pressure of 1×10^4 Pa and 2×10^3 Pa, respectively. The oxygen partial pressure could be obtained by controlling the oxygen flux. Zeng et al. [38] also studied the effect of oxygen partial pressure on Sb_2O_3 nanoparticles, where two oxygen partial pressures of 0.5×10^3 Pa and 4×10^3 Pa were selected. After the required oxygen partial pressure was maintained for 20 min, the bulk Sb was heated by an inductive resource to its melting point. Subsequently, the laser beam was focused

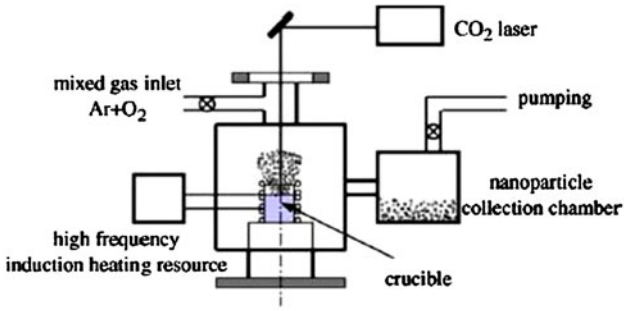

Fig. 15 Schematic diagram of the experimental HILH setup for the synthesis of the nanoparticles [38]

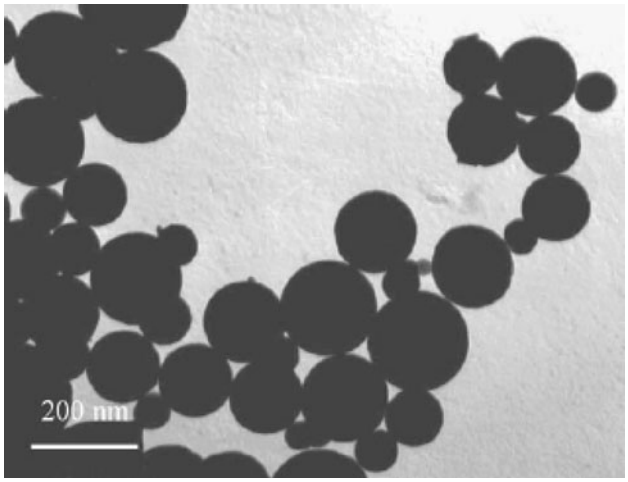

Fig. 16 TEM image of the Sb_2O_3 nanoparticles obtained by HILH method [37]

on the Sb liquid surface under normal incidence. It was observed that the absorption coefficient of the molten metal liquid to laser was much higher as compared to the solid metal [84]. Thus, melting the pure solid Sb by induction heating resource first and subsequently laser irradiation on the liquid Sb increased the yield rate of the Sb_2O_3 nanoparticles. The Sb_2O_3 nanoparticles could be obtained via the reaction of the evaporated Sb clusters from the liquid surface with the O_2 gas, which was channeled away toward the nanoparticles collection chamber.

Figure 16 depicts the Sb_2O_3 nanoparticles in spherical shape with an average size of approximately 80 nm (sizes ranging from 50 to 180 nm), which is a similar finding to the γ-ray radiation–oxidation route [33]. The size distributions are mainly bimodal, where two categories: 60–70 and 120–140 nm are identified. The second category is caused by the tendency of the small particles to agglomerate and subsequently form larger nanoparticles (>100 nm). TEM images of nanoparticles at 0.5×10^3 Pa and 4×10^3 Pa as shown in Fig. 17 indicate that the nanoparticles are spherical in shape with sizes ranging from 40 to 150 nm. At a higher oxygen partial pressure (4×10^3 Pa), there exist only a few irregular polyhedron Sb_2O_3 nanoparticle which marked by "A" as shown in Fig. 17b.

Figure 18 shows XRD spectrum of the Sb_2O_3 nanoparticles at three different oxygen partial pressures, where two phases: pure Sb and its oxide Sb_2O_3 are observed. It revealed that the Sb-to-Sb_2O_3 ratio of the relative diffraction peak intensity decreased remarkably with increasing oxygen partial pressure. In other words, it could be explained that pure Sb elements decreased significantly when higher oxygen partial pressure was applied. The size of the Sb_2O_3 nanoparticles was calculated using the Scherrer equation [85]. The calculated average size of the

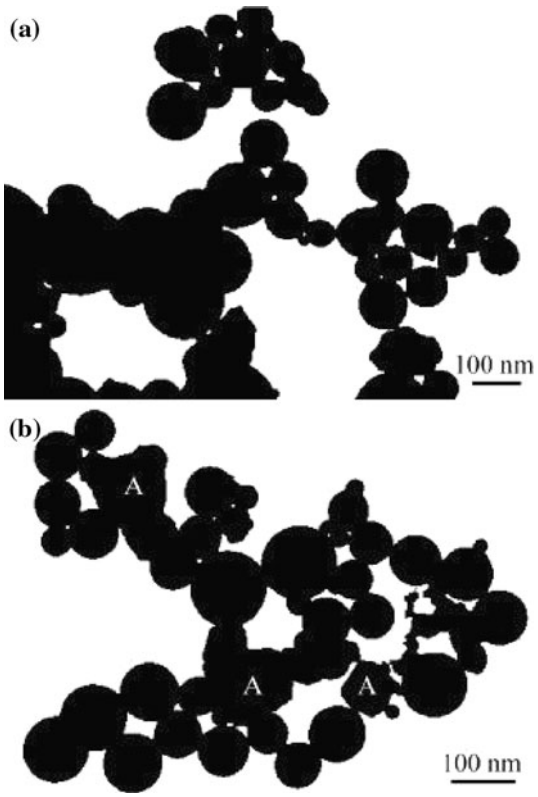

Fig. 17 TEM image of the Sb_2O_3 nanoparticles under different oxygen partial pressure: **a** 0.5×10^3 Pa and **b** 4×10^3 Pa [38]

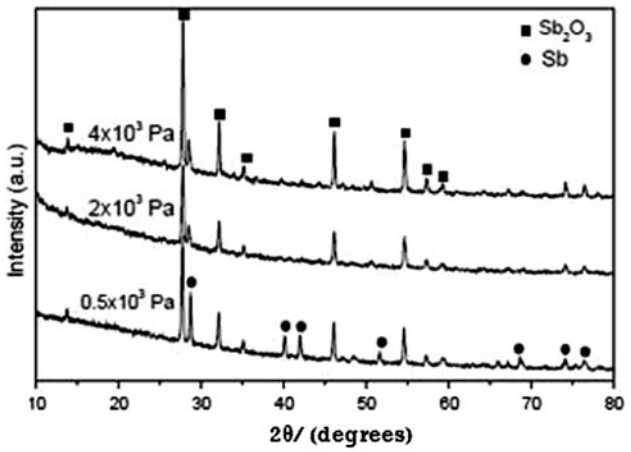

Fig. 18 XRD spectrum of Sb_2O_3 nanoparticles at 0.5×10^3 Pa, 2×10^3 Pa, and 4×10^3 Pa [38]

Sb_2O_3 nanoparticles was ~60 nm, which was consistent with the low particle size distribution observed in the TEM images.

In summary, Sb_2O_3 nanoparticles were successfully synthesized via the HILH method from pure Sb in the atmosphere of a flowing mixture of Ar + O_2 gas under different oxygen partial pressures [37, 38]. The Sb_2O_3 nanoparticles are in spherical shape with an average size of ~80 nm. Furthermore, the HILH method can be applied to a larger-scale production of nanoparticles due to the high absorption characteristic of the metallic liquid to the CO_2 laser [26]. In addition, oxygen partial pressure is one of the key parameters to control the formation and stability of the Sb_2O_3 nanoparticles. Higher oxygen partial pressure caused metallic Sb element in the nanoparticles to decrease significantly.

Thermal oxidation

Xu et al. [43] discovered the synthesis of pure Sb_2O_3 nanoparticles by heating metal Sb in its solid state in an oxidizing environment and collecting Sb_2O_3 vapor on the substrate at the downstream of the gas flow. The purpose of exploring this method is to overcome the limitation of the HILH method, where the mixture of Sb and Sb_2O_3 nanoparticles are usually obtained via the HILH method [26, 38]. Figure 19 shows the experimental setup for the synthesis Sb_2O_3 nanoparticles by the thermal oxidation method. The experiment started by putting commercial granular Sb with an average diameter of 1.5 mm (purity: 99.99% Sb) in an alumina crucible. Sb granular in the alumina crucible was placed in the middle of a tube furnace in compressed air at a pressure of 1 atm with a constant flow rate of 400 mL/min for 4 and 20 h. The temperature at the center of the furnace where the sample was placed was set at 550 °C (melting point of Sb is 630.5 °C). Aluminum (Al)-foil substrate was put in the downstream of gas flow (250 °C) to collect Sb_2O_3 nanoparticles. The Sb_2O_3 nanoparticles deposited on the substrates were in white color.

SEM images revealed that the size of Sb_2O_3 nanoparticles ranges from 10 to 100 nm after deposition of 4 h and 150 to 250 nm after deposition of 20 h as illustrated in Fig. 20. As the deposition time increased, the size of nanoparticles increased accordingly. Those large particles are in polyhedral shape, such as triangular, hexagonal, and rectangular shape, with well-defined crystal structures, while the small ones tend to be round in shape. Figure 19

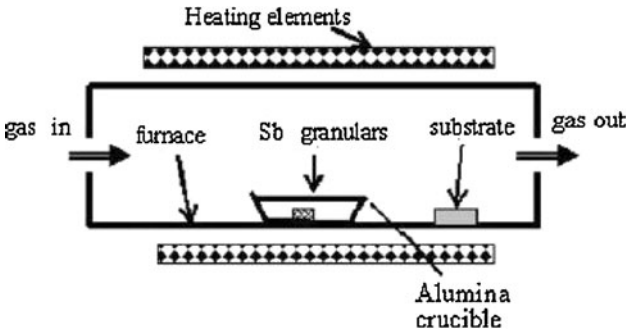

Fig. 19 Experimental setup shows the position of granular antimony and the substrates [43]

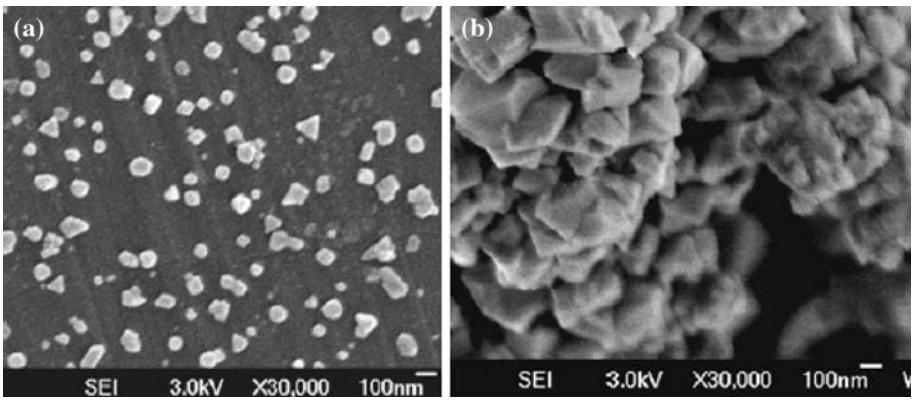

Fig. 20 TEM images of the Sb_2O_3 deposited on Al-foil substrate, showing size of nanoparticles **a** about 10–100 nm after the reaction of 4 h and **b** 150–250 nm after the reaction of 20 h [43]

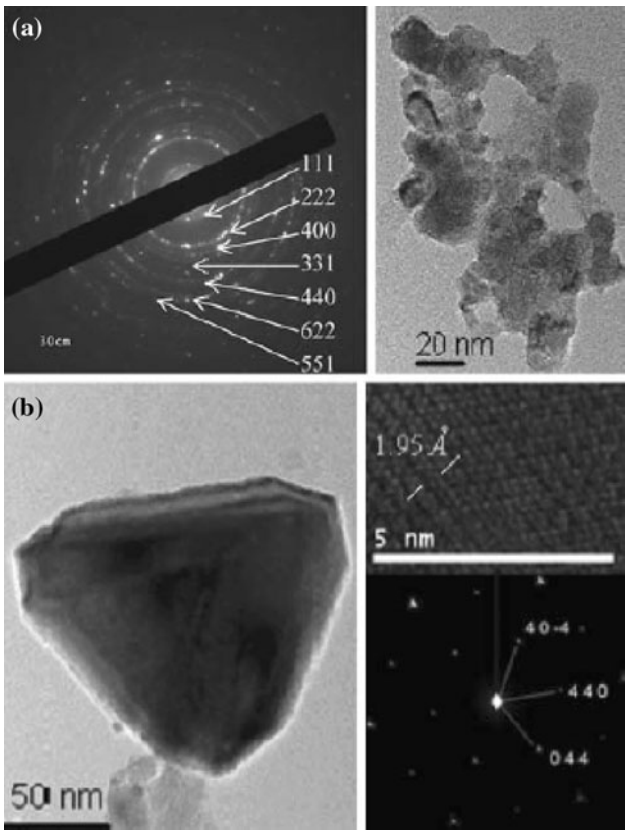

Fig. 21 TEM images for Sb_2O_3 particles **a** the morphology of a pile of Sb_2O_3 (*right*) and the corresponding SAED pattern (*left*), **b** the morphology of a large triangle grain (*left*), the corresponding SAED pattern (*right bottom*) and the related high-resolution image taken on the triangle Sb_2O_3 (*right top*) [43]

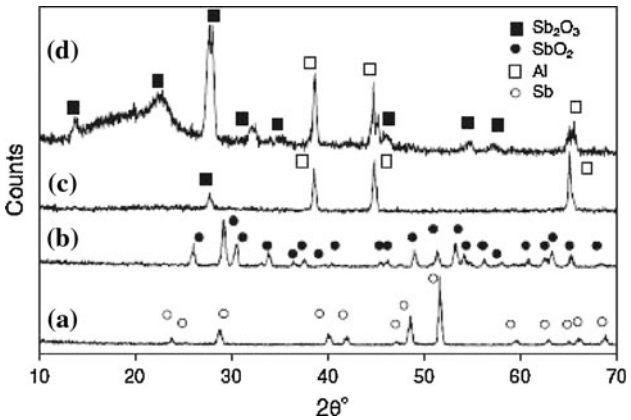

Fig. 22 XRD spectrum **a** granular Sb before the reaction, **b** the oxidized granular Sb in the alumina crucible after the reaction of 4 h, showing SbO_2 oxide, **c** the deposited oxide on Al-foil after the reaction of 4 h, and **d** the deposited oxide on Al-foil after the reaction of 20 h, showing Sb_2O_3 [43]

shows TEM images of Sb_2O_3 nanoparticles with grain size ranging from 10 to 100 nm. A pile of Sb_2O_3 and the corresponding SAED pattern are shown in Fig. 21a, where all rings can be indexed to the diffraction peaks of FCC Sb_2O_3. Figure 21b displays a large triangular shape of the grain and its corresponding SAED pattern. The SAED pattern comes from Sb_2O_3, indicating that the triangular surface is the (111) surface of Sb_2O_3. The lattice space of 1.95 Å obtained from the high-resolution TEM examination on the triangular Sb_2O_3, corresponds to the (440) plane of Sb_2O_3.

Figure 22 shows the XRD spectrum of granular Sb and oxidized granular Sb deposited on the substrates after 4 and 20 h. Before reaction, pure Sb with a rhombohedral structure was examined and the result is illustrated in Fig. 22a. After deposition of 4 h, the oxidized granular Sb in the alumina crucible formed an orthorhombic structure of SbO_2, which is shown in Fig. 22b. Figure 22c displays the XRD spectrum of oxide deposited on the Al foil after 4 h, the Al peaks dominated while only one oxide peak presents in a small amount and the phase of the oxide is hard to be identified. The oxide particles deposited on Al foil after 20 h exhibit a pure cubic (FCC) structure of Sb_2O_3 (without the presence of metallic Sb), which is shown in Fig. 22d.

From this method, pure Sb_2O_3 nanoparticles with size ranges 10–100 nm can be synthesized by heating metallic Sb at 550 °C under a pressure of 1 atm in a constant air flow rate 400 mL/min [43]. The cubic (FCC) Sb_2O_3 nanoparticles are deposited on a substrate at the

downstream of gas flow. Comparing to the HILH method, the present method is able to synthesis pure Sb_2O_3 nanoparticles in a more cost-effective manner.

Starting material: slag

Vacuum evaporation method

Qiu and Zhang [44] investigated the synthesis of Sb_2O_3 nanoparticles from slag-containing Sb via a vacuum evaporation method. Particle size and whiteness of Sb_2O_3 are influenced by temperature, time, and pressure depending on the evaporation rate of Sb. The starting materials, which was slag, consisted of 39.49 wt% Sb, 27.87 wt% lead (Pb), 7.45 wt% Tin (Sn), and 2.33 wt% iron (Fe). The main phase compositions of Sb, Pb, and Sn were Sb_2O_3, PbO, and SnO_2, respectively. The slag was placed in the vacuum chamber and was heated to a certain temperature by an electric heater, and then the timing of the thermal evaporation process was started. A series of experimental conditions including evaporation temperature, residual pressure, and time were carried out to obtain the optimum process conditions for preparing the desired particle size and whiteness of the Sb_2O_3 nanoparticles (Table 7). A thermoelectric couple was connected with a temperature-controlling device. The slag was evaporated in the vacuum chamber, and Sb_2O_3 nanoparticles were collected from the condensation cavity. The basic principle of separating Sb_2O_3 from slag is due to the difference in vapor pressure of each substance in the slag at a temperature, which is presented in Table 8. From Table 8, the saturation vapor pressure of both PbO and SnO_2 is low, which are 5.67 and 1 Pa, respectively. Thus, Sb_2O_3 with higher vapor pressure evaporates into gas phase, while PbO and SnO_2 remain in residual liquid or residue.

Table 7 Experimental results under various conditions [44]

Sample	Temperature (K)	Pressure (Pa)	Time (h)	Whiteness (%)	Average particle size (nm)
1	893	250	1	91.2	64
2	993	250	1	82.4	86
3	1043	250	1	75.7	N/A
4	1093	250	1	70.6	N/A
5	893	65	2	89.4	N/A
6	893	250	2	90.0	72
7	893	450	2	90.4	77
8	893	650	2	90.7	84
9	993	250	0.5	82.8	N/A
10	993	250	2	81.9	91

Table 8 Relationships between saturation vapor pressure of Sb_2O_3 and PbO and values of $P^0_{Sb_2O_3}/P^0_{PbO}$ and temperature [44]

T (K)	$P^0_{Sb_2O_3}$ (Pa)	P^0_{PbO} (Pa)	$P^0_{Sb_2O_3}/P^0_{PbO}$
893	458.91	0.02	22945.50
943	1331.26	0.13	10240.46
993	2150.34	0.63	3413.24
1043	3317.31	2.59	1280.81
1073	4220.18	5.67	744.30

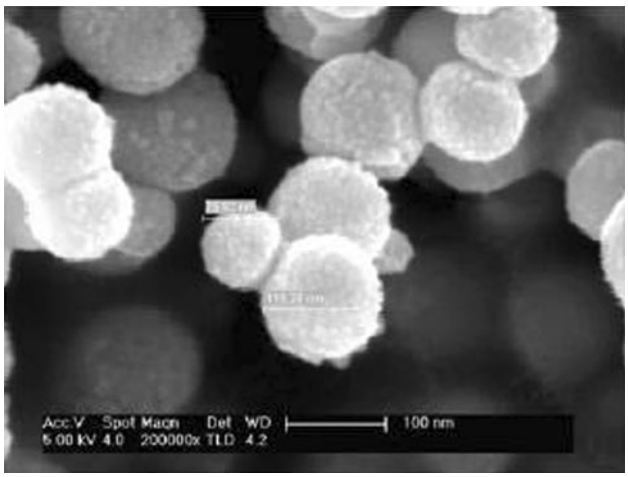

Fig. 23 SEM image of Sb_2O_3 nanoparticles with mean particle size ~100 nm obtained by vacuum evaporation method [44]

The SEM image in Fig. 23 shows Sb_2O_3 nanoparticles are spherical in shape with particle sizes ranging from 45 to 140 nm and mean sizes of approximately 100 nm. On the other hand, the XRD spectrum of pure cubic (FCC) structure of Sb_2O_3 nanoparticles is observed in Fig. 24. Moreover, there are no other impurities which are detected

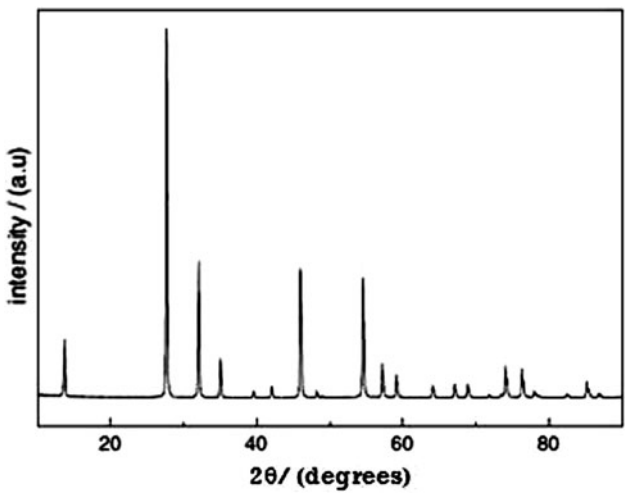

Fig. 24 XRD spectrum of Sb_2O_3 nanoparticles obtained by vacuum evaporation method [44]

from the spectrum and the average particle size calculated using the Scherrer equation is 40 nm.

In conclusion, pure spherical shapes of Sb_2O_3 nanoparticles with cubic (FCC) structure and an average particle size of 72 nm were synthesized successfully via the vacuum evaporation method of slag under optimum experimental conditions [44]. The optimum experimental conditions are evaporation temperature 893 K and pressure 250 Pa for 2 h. Results revealed that the average particle size of Sb_2O_3 nanoparticles increased with increasing temperature, while the whiteness of Sb_2O_3 nanoparticles decreased with increasing temperature. Furthermore, lowering the pressure will decrease the average particle size of Sb_2O_3, which is the basic concept for synthesis Sb_2O_3 nanoparticles. The advantages of this method are simple technological flow sheet, no or less environmental pollution, less floor area, low consumption of energy and raw material, and good economic effects [44].

Applications

In general, OA nanoparticles have been widely used in numerous industries over the past decade. It can be categorized into three main fields; chemical, sensing, and semiconducting. Details of each field are reviewed in the subsequent paragraphs.

Chemical

The main applications of OA nanoparticles are as a flame-retardant synergist in plastics, paints, adhesives, sealants, rubber, and textile back coatings [45–51, 86–94]. Flame retardants can be defined as chemicals that help to slow down the combustion reaction of polymers [95]. The flame-retardant synergist will only start to function when combined with halogenated compounds, such as chlorine or bromine-based compounds. There are a few properties of the OA nanoparticles which contribute to this application, which are high heat stability, covering power, and transparency [96]. Literature [97] reported that the senarmontite phase (cubic polymorph of Sb_2O_3) has long been used as an additive to enhance the flame retardancy of polymer resins, whereas valentinite phase (orthorhombic polymorph of Sb_2O_3) has not due to its undesirable oxidation when exposed to air or sunlight. Although halogenated flame retardants are highly effective for reducing the heat release rate of commodity thermoplastics, the future use of these flame retardants has raised environmental concerns in Europe [91]. Therefore, Laachachi et al. [48] investigated the influence of Sb_2O_3 on the thermal stability and flammability properties of poly(methyl methacrylate) (PMMA), as one of the halogen-free flame retardants. Results indicated that both the thermal stability and the flammability properties of PMMA were improved when incorporated with a certain amount of Sb_2O_3.

OA nanoparticles also possess excellent catalytic performance in PET and organic synthesis industries. In the PET industry, Sb_2O_3 plays the role of a catalyst to produce PET plastic which is used in the packaging of mineral water and soft drinks [52–56]. OA is a favorable polycondensation catalyst because it possesses a high catalytic activity, does not create unwanted colors, and has a low affinity to catalyze side reactions. In addition, OA acts as a catalytic agent in organic synthesis, especially when combined with uranium, molybdenum oxide, or iron oxide for propane ammoxidation and propene oxidation and ammoxidation [52, 54, 55, 98]. Research [54] has shown that the senarmontite phase (cubic polymorph of Sb_2O_3) also acts as a catalyst in combination with vanadium for the selective oxidation of *o*-xylene. Besides, antimony dioxide (Sb_2O_4) works as a catalyst together with other oxides for hydrocarbon cracking, hydrogen reduction, and producing ceramic materials. Matsumura et al. [56] reported that the mixture of molybdenum oxide (MoO_3) and α-Sb_2O_4 showed high performance in the selective oxidation of methanol to formaldehyde.

Legouera et al. [57] reported that OA is widely used as a clarifying or refining agent in optical glass, television's tube, lighting (bulbs and tube lights), and crystal manufacturing, where it helps to remove bubbles during production. It also acts as an opacifier to densify porcelain, enamel, and low fire glazes [59]. At the same time, it works as a filling or covering agents and retardants for rubber, ceramics, enamels, fabrics, and fiber products [60]. Additionally, it is used as pigments and retardants in oil paint and coating material industry in conjunction with its white pigment property [35]. From a medicinal perspective, Sb_2O_3 or Sb_2O_5 is well known to be a potential chemical for the synthesis of antimony gluconate, which is believed to be the effective medicine to cure the Kala azar (*Visceral Leishmaniasis*) disease [35].

Sensing

Recently, some researchers [23, 24] have reported that hydrous Sb_2O_3 exhibits high proton conductivity, which is potentially useful in humidity-sensing material. In fact, Sb_2O_3 [70] and Sb_2O_3 plus ZnO [99] have been applied to create films for gas-sensing purposes [100]. Preliminary reports [101] discovered that a small response to methane gas (resistance decreased by 15%) and some recovery on the removal of the gas exist when using OA as a gas sensor. Nevertheless, this report observed a dramatic change in resistance of the baseline (resistance increased by 25%) over a 15-min period than the actual sensor response.

Hence, Binions et al. [70] have successfully prepared gas sensors by the atmospheric pressure chemical vapor deposition (APCVD) and screen printed method, which is useful for reducing gases, such as ethanol at an operating temperature of 400 and 500 °C, respectively.

Semiconducting

Semiconducting of V and VI compounds have potential in optical, electronic, and optoelectronic applications. Among them, Sb_2O_3 is a crucial compound and predominantly interesting, due to its large and indirect bandgap situated near the UV region [68]. In conjunction with that, it is also an amazing UV filter for interferometric applications, as well as applied in UV light emitting device (LED) and solar cell technology [22, 68]. Moreover, OA nanoparticles are considered as one of the important optical materials because of their high refractive index and high abrasive resistance [21, 22]. Literature [69] reviewed that the valentinite phase, which is an orthorhombic polymorph of Sb_2O_3, is the main element of the Sb_2O_3–B_2O_3 binary glasses that has nonlinear optical properties.

Conclusion

In conclusion, there are total of eight synthesis methods to synthesis oxides of antimony nanoparticles which have been reviewed. They are discussed in term of their properties and applications. Among them the biosynthesis method using yeast as staring material is able to synthesis the smallest size (2–10 nm) and uniformly distributed particles in spherical shape. However, it requires a longer processing time ($\sim$6 h). Therefore, more efforts are needed to seek a synthesis method that is capable to produce uniformly dispersed and smaller sized (<10 nm) nanoparticles in a shorter time at a relatively lower cost. Thus, it is believed that these improvements may lead to the mass commercialization for future applications.

Acknowledgements The first author (H.S.C.) would like to express her appreciation to the USM RU-PRGS grant and USM Fellowship for the scholarship and financial support on this project. The second author (K.Y.C.) would like to acknowledge financial support given by USM Short Term Grant (6039038).

References

1. Iwanaga H, Fujii M, Takeuchi S (1998) J Cryst Growth 183:190
2. Linderoth S, Pedersen MS (1994) J Appl Phys 75:5867
3. Gleiter H (1989) Prog Mater Sci 33:223
4. Salata OV (2004) J Nanobiotechnol 2:1
5. Cao Y, Jin R, Mirkin CA (2001) J Am Chem Soc 123:7961
6. Morales AM, Lieber CM (1998) Science 279:208
7. Bley RA, Kauzlarich SM (1996) J Am Chem Soc 118:12461
8. Han WQ, Fan SS, Li QQ, Hu YD (1997) Science 277:1287
9. Pan ZW, Dai ZR, Wang ZL (2001) Science 291:1947
10. Wang X, Li YD (2006) Inorg Chem 45:7522
11. Xia YN, Yang PD, Sun YG, Wu YY, Mayers B, Gates B, Yin YD, Kim F, Yan HQ (2003) Adv Mater 15:353
12. Zeng HC (2006) J Mater Chem 16:649
13. Rao CNR, Deepak FL, Gundiah G, Govindaraj A (2003) Prog Solid State Chem 31:5
14. Jun YW, Choi JS, Cheon J (2006) Angew Chem Int Ed 45:3414
15. Huang MH, Mao S, Feick H, Yan HQ, Wu YY, Kind H, Weber E, Russo R, Yang PD (2001) Science 292:1897
16. Massalski TB, Okamoto H, Subramanian PR, Kacprzak L (1990) Binary alloy phase diagrams. ASM International, Materials Park
17. Xu CH, Gao W, He YD (2000) Scripta Mater 42:975
18. Xu CH, Woo CH, Shi SQ (2004) Chem Phys Lett 399:62
19. Khanna AS (2002) Introduction to high temperature oxidation and corrosion. ASM International, Materials Park
20. Samsonov GV (1973) The oxide handbook. IFI/Plenum, New York
21. Nalin M, Messaddeq Y, Ribeiro SJL, Poulain M, Briois V (2001) J Optoelectron Adv Mater 3:553
22. Sahoo NK, Apparao KVSR (1997) Appl Phys A 63:195
23. Ozawa K, Sakka Y, Amano M (1998) J Mater Res 13:830
24. Dzimitrowicz DJ, Goodenough JB, Wiseman PJ (1982) Mater Res Bull 17:971
25. Chang PR, Yu J, Ma X (2009) Macromol Mater Eng 294:762
26. Xie CS, Hu JH, Wu R, Xia H (1999) Nanostruct Mater 11:1061
27. Zhang ZL, Guo L, Wang WD (2001) J Mater Res 16:803
28. Ye CH, Wang GY, Kong MG, Zhang LD (2006) J Nanomater 2006:1
29. Edelstein AS, Cammarata RC (1996) Nanomaterials: synthesis, properties and applications. Institute of Physics, Bristol
30. Zhang JR, Gao L (2004) Mater Chem Phys 87:10
31. Toraya H, Yoshimura M, Somiya S (1983) J Am Ceram Soc 66:148
32. Chen XY, Huh HS, Lee SW (2008) J Solid State Chem 181:2127
33. Liu YP, Zhang YH, Zhang MW, Zhang WH, Qian YT, Yang L, Wang CS, Chen ZW (1997) Mater Sci Eng B 49:42
34. Liu YP, Qian YT, Zhang MW, Chen ZY, Wang CS (1996) Mater Lett 26:81
35. Jha AK, Prasad K (2009) Biochem Eng J 43:303
36. Jha AK, Prasad K (2009) J Biotechnol 4:1582
37. Zeng DW, Xie CS, Zhu BL, Song WL (2004) Mater Lett 58:312
38. Zeng DW, Zhu BL, Xie CS, Song WL, Wang AH (2004) Mater Sci Eng A 366:332
39. Siegel RW (1994) Nanostruct Mater 4:121
40. Wu R, Xie CS, Hu JH, Xia H, Wang AH (2000) Scripta Mater 43:841
41. Wu R, Xie CS, Xia H, Hu JH, Wang AH (2000) J Cryst Growth 217:274
42. Tigau N, Ciupina V, Prodan G, Rusu GI, Vasile E (2004) J Cryst Growth 269:392
43. Xu CH, Shi SQ, Surya C, Woo CH (2007) J Mater Sci 42:9855. doi:10.1007/s10853-007-1799-z
44. Qiu KQ, Zhang RL (2006) Vacuum 80:1016
45. Pillep B, Behrens P, Schubert UA, Spengler J, Knozinger H (1999) J Phys Chem B 103:9595
46. Jakab E, Uddin MA, Bhaskar T, Sakata Y (2003) J Anal Appl Pyrolysis 68–69:83
47. Jang J, Lee E (2000) Polym Test 20:7
48. Laachachi A, Cochez M, Ferriol M, Leroy E, Lopez Cuesta JM, Oget N (2004) Polym Degrad Stab 85:641
49. Xie XL, Li RKY, Liu QX, Mai YW (2004) Polymer 45:2793

50. Brebua M, Jakab E, Sakata Y (2007) J Anal Appl Pyrolysis 79:346
51. Sato H, Kondo K, Tsuge S, Ohtani H, Sato N (1998) Polym Degrad Stab 62:41
52. Duh B (2002) Polymer 43:3147
53. Nanda KK, Sahu SN, Behera SN (2002) Phys Rev A - At Mol Opt Phys 66:132081
54. Spengler J, Anderle F, Bosch E, Grasselli RK, Pillep B, Behrens P, Lapina OB, Shubin AA, Eberle HJ, Knozinger H (2001) J Phys Chem B 105:10772
55. Liu H, Imoto H, Shido T, Iwasawa Y (2001) J Catal 200:69
56. Matsumura H, Okumura K, Shimamura T, Ikenaga N, Miyake T, Suzuki T (2006) J Mol Catal A 250:122
57. Legouera M, Kostka P, Poulain M (2004) J Phys Chem Solids 65:901
58. Cox DM, Trevor DJ, Whetten RL, Rohlfing EA, Kaldor A (1985) Phys Rev B 32:7290
59. Zhang YX, Li GH, Zhang J, Zhang LD (2004) Nanotechnology 15:762
60. Deng Z, Tang F, Chen D, Meng X, Cao L, Zou B (2006) J Phys Chem B 110:18225
61. Remy H (1956) Treatise on inorganic chemistry. Elsevier, Amsterdam
62. Whitten AE, Dittrich B, Spackman MA, Turner P, Brown TC (2004) Dalton Trans 1:23
63. Svensson C (1974) Acta Crystallogr B 30:458
64. Svensson C (1975) Acta Crystallogr B 31:2016
65. Amador J, Gutierrez Puebla E, Monge MA, Rasines I, Ruiz Valero C (1988) Inorg Chem 27:1367
66. Liu KS, Zhai J, Jiang L (2008) Nanotechnology 19:165604
67. Nyffenegger RM, Craft B, Shaaban M, Gorer S, Erley G, Penner RM (1998) Chem Mater 10:1120
68. Tigau N, Ciupina V, Prodan G (2005) J Cryst Growth 277:529
69. Terashima K, Hashimoto T, Uchino T, Kim SH, Yoko T (1996) J Ceram Soc Jpn 104:1008
70. Binions R, Carmalt CJ, Parkin IP (2006) Polyhedron 25:3032
71. Xiang S, Yang X, Cao T (2000) Nitrogen, phosphorus, and arsenic subgroup. Scientific Press, Beijing
72. Pinna N, Weiss K, Sack-Kongehl H, Vogel W, Urban J, Pileni MP (2001) Langmuir 17:7982
73. Wang L, Tomura S, Ohashi F, Maeda M, Suzuki M, Inukai K (2001) J Mater Chem 11:1465
74. Leontidis E, Kyprianidou-Leodidou T, Caseri W, Kyriacou KC (1999) Langmuir 15:3381
75. Pileni MP (2001) J Phys Chem B 105:3358
76. Cao M, Hu C, Wang Y, Guo Y, Guo C, Wang E (2003) Chem Commun 9:1884
77. Biz S, Occelli ML (1998) Catal Rev Sci Eng 40:329
78. Ye C, Fang X, Wang Y, Xie T, Zhao A, Zhang L (2004) Chem Lett 33:54
79. Wang YL, Jiang XC, Xia YN (2003) J Am Chem Soc 125:16176
80. Scott RWJ, Coombs N, Ozin GA (2003) J Mater Chem 13:969
81. Kempf JY, Maigret B, Crans DC (1996) Inorg Chem 35:6485
82. Langford JI, Wilson AJC (1978) J Appl Cryst 11:102
83. Wagner CNJ, Aqua EN (1964) Adv X-ray Anal 7:46
84. Lu J, Ni XW, He AZ (1994) Physics of laser-materials interaction. Mechanical Industry Press Corp, Beijing
85. Klug HP, Alexander E (1954) X-ray diffraction procedures for polycrystalline and amorphous materials. Wiley, New York
86. Feng L, Wang J, Liu J, Wang B, Song S (2007) J Compos Mater 41:1487
87. Feng L, Liu J, Liao L, Wu J (2005) J Chem Ind Eng 56:2245
88. Chiang WY, Hu CH (1999) J Appl Polym Sci 71:865
89. Owen SR, Harper JF (1999) Polym Degrad Stab 64:449
90. Seddon R, Harper JF (2001) Macromol Symp 169:109
91. Montezin F, Lopez Cuesta JM, Crespy A, Georlette P (1997) Fire Mater 21:245
92. Tai CM, Li RKY (2001) J Appl Polym Sci 80:2718
93. Brebu M, Bhaskar T, Murai K, Muto A, Sakata Y, Uddin MA (2004) Polym Degrad Stab 84:459
94. Karak N, Maiti S (1998) J Appl Polym Sci 68:927
95. Mostashari SM, Baie S (2008) J Therm Anal Calorim 94:97
96. Zhao J, Wang X, Liu C, Xu X, Li Y (2008) Powder Technol 183:220
97. Bernett RD, Mitchell A, Brown TC (2004) J Mater Sci 39:1075. doi:10.1023/B:JMSC.0000012947.67817.17
98. Liu H, Iwasawa Y (2002) J Phys Chem B 106:2319
99. Zhu BL, Xie CS, Wang AH, Zeng DW, Hu ML, Wang WY (2004) Mater Res Bull 39:409
100. Badawy WA, El-Taher EA (1988) Thin Solid Films 158:277
101. Bae JS, Yun DH, Park CO, Hwang JS (2001) Sens Actuators B 75:160